

Interface Engineering Ti_3C_2 MXene/Silicon Self-Powered Photodetectors with High Responsivity and Detectivity for Weak Light Applications

Weidong Song,* Qing Liu, Jiaxin Chen, Zhao Chen, Xin He, Qingguang Zeng, Shutu Li, Longfei He, Zhitao Chen, and Xiaosheng Fang*

Interfacial engineering and heterostructures designing are two efficient routes to improve photoelectric characteristics of a photodetector. Herein, a Ti_3C_2 MXene/Si heterojunction photodetector with ultrahigh specific detectivity (2.03×10^{13} Jones) and remarkable responsivity (402 mA W^{-1}) at zero external bias without decline as with increasing the light power is reported. This is achieved by chemically regrown interfacial SiO_x layer and the control of Ti_3C_2 MXene thickness to suppress the dark noise current and improve the photoresponse. The photodetector demonstrates a high light on/off ratio of over 10^6 , an outstanding peak external quantum efficiency (EQE) of 60.3%, while it maintains an ultralow dark current at 0 V bias. Moreover, the device holds high performance with EQE of over 55% even after encapsulated with silicone, trying to resolve the air stability issue of Ti_3C_2 MXene. Such a photodetector with high detectivity, high responsivity, and self-powered capability is particularly applicable to detect weak light signal, which presents high potential for imaging, communication and sensing applications.

1. Introduction

To construct two-dimensional materials (2DMs)/bulk semiconductor van der Waals (vdW) heterojunctions is an efficient way to build high-performance photodetectors (PDs).^[1–3] The

atomic thin 2D vdW heterojunction is fully compatible with various amorphous or crystalline substrates due to the weak interface bonding, while needless to consider the lattice mismatching condition as with conventional hetero-epitaxy.^[4–6] Moreover, even a small depletion area can fully deplete the very thin photosensitive 2D crystals, thereby ensuring high-speed light response.^[7,8] For optoelectronics, this platform makes up for the weakness of low light absorption of atomic thin layers through the bulk absorption, pointing toward the high-efficiency photo-to-electric conversion. In recent times, using semi-metallic graphene or 2D metals (or 2D semimetals), researchers have developed a wealth of 2DMs/bulk semiconductor (Si, Ge, GaAs, GaN etc.) vdW heterostructures to construct Schottky barrier junction photodiodes.^[9–13] In this type of photodiodes, the bulk semiconductors absorb photons to generate electron-hole pairs, and the 2DMs act as transparent Schottky electrodes to collect the photoinduced carriers. The photoexcited electron-hole pairs are immediately and efficiently separated by the built-in electric field at the adjacent interface between 2DMs and the underlying semiconductors, resulting in photocurrent as a function of incident light power.^[10] It has been reported that the graphene/Si photodiode with ultra-shallow junction possesses internal quantum efficiency approaching the upper-limit of Si based ultraviolet PDs.^[14] Nevertheless, the complex transfer process for the fabrication of vdW heterojunction PDs hinders their applications for large-scale, high-integration devices.^[7]

As a new member of 2DMs family, 2D transition metal carbides (denoted as MXenes) have emerged as a new material star for many applications in electronics and optoelectronics, due to their unique metallic conductivity and hydrophilic surfaces, not to mention that their (opto)electronic performances can be further modified by fruitful surface functional groups and transition metals.^[15–20] Most importantly, MXenes are solution-processable via routes such as spin-coating, drop-casting, spray, inkjet printing etc., which provides strong support for large-scale, low-cost integration production.^[21–24] The excellent electronic and optical properties of MXenes enable them to play rich roles in optoelectronics, such as transparent electrodes, Schottky contacts, light absorbers, and plasma materials.^[17,18] Recently, a Ti_3C_2 MXene/Si solar cell with a maximum power

Dr. W. D. Song, Z. Chen, Prof. X. He, Prof. Q. G. Zeng
College of Applied Physics and Materials
Wuyi University


22 Dongcheng Village, Jiangmen 529020, P. R. China
E-mail: wdsongwyu@163.com

Dr. W. D. Song, J. X. Chen, Prof. X. S. Fang
Department of Materials Science

Fudan University
Shanghai 200433, P. R. China
E-mail: xshfang@fudan.edu.cn

Dr. Q. Liu, Prof. S. T. Li
Guangdong Engineering Research Center of Optoelectronic Functional
Materials and Devices
Institute of Semiconductors
South China Normal University
Guangzhou 510631, P. R. China

Dr. L. F. He, Prof. Z. T. Chen
Guangdong Institute of Semiconductor Industrial Technology
Guangdong Academy of Sciences
Guangzhou 510650, P. R. China

 The ORCID identification number(s) for the author(s) of this article can be found under <https://doi.org/10.1002/smll.202100439>.

DOI: 10.1002/smll.202100439

conversion efficiency of 11.5% has been developed.^[25] Nabet and co-workers found that spin-coated Ti_3C_2 film as a Schottky electrode to fabricate GaAs PDs outperformed the noble metal gold electrode, including the photoresponsivity, quantum efficiency, and specific detectivity.^[24] Gao et al. reported a $\text{Ti}_3\text{C}_2/\text{Si}$ PD by a simple drop-casting method, which is a self-powered device aiming at energy saving electronics. Nevertheless, as with those commonly reported 2DMs/Si photodiodes, they exhibit fast response speed and wide dynamic range, but the responsivity (26.95 mA W^{-1}) and detectivity are relatively low, which limit practical applications.^[22] Generally, the interface between 2DMs and Si contains a relatively high density of surface states. These energy states are related to photogenerated carrier recombination, which plays a destructive role for the aim to achieve highly responsive PDs. On the other hand, these surface states tend to pin the surface Fermi levels of Si. This indicates that a low Schottky barrier may be formed between Si and 2DMs, which is insensitive to the work functions (WFs) of 2DMs.^[26,27] As a result, a large dark leakage current (background noise current) is formed, limiting the specific detectivity of 2DMs/Si PDs.^[28] Therefore, the performances of 2DMs/Si heterojunction optoelectronic devices are mainly depend on the quality of the interface, which is worth for further exploring.

It is known that the Fermi level pinning is originated from the dangling bonds on Si surface that introduces energy states inside the surface band gap. Introducing a high-quality passivation dielectric layer at the heterointerface is an effective way to alleviate this problem. Smith et al. found that a chemically grown SiO_x on Si surface effectively improved the photovoltage and barrier height of a n-Si/ SiO_x /Pt/Ni photoanode for high-efficiency photoelectrochemical water splitting. And it was attributed to the high quality of surface chemical passivation by the chemically modified surface.^[29] In this study, we introduced a chemically regrown interfacial oxide layer to suppress

the dark current noise and improve the photoresponse simultaneously in a Ti_3C_2 MXene/ SiO_x /n-Si photodiode. Compared with the devices with naturally grown oxide interface, the photocurrent of the chemically oxidized devices is enhanced by two orders of magnitude; while the dark current is reduced by an order of magnitude compared with the oxide removed devices. Meanwhile, the photodetection performances are further improved by controlling the thickness of the spray coated Ti_3C_2 film to balance its conductivity and light absorption. The device exhibits remarkable photodetection capabilities at room temperature, including self-powered working ability, excellent peak responsivity (402 mA W^{-1}), external quantum efficiency (>60%), and outstanding specific detectivity (over 10^{13} Jones). The high detectivity ensures the device to detect weak light power as low as 58 nW (instrumental limit) with on/off ratio maintaining three orders of magnitudes. Moreover, the silicone-encapsulated $\text{Ti}_3\text{C}_2/\text{SiO}_x$ /n-Si photodiode can reserve detectivity and EQE values of nearly 100% and 90% relative to their naked devices, respectively, while providing stable and repeatable photodetection. These results indicate that the Ti_3C_2 /n-Si vdW heterojunction photodiode with facile interfacial engineering has high application potential, especially for developing highly performing weak light signal PDs.

2. Results and Discussion

Figure 1a presents a typical scanning electron microscope (SEM) image of as-delaminated Ti_3C_2 nanosheet by etching the precursor Ti_3AlC_2 powder. The observed fold-like microstructure morphology indicates the successful exfoliation of thin few-layered Ti_3C_2 nanosheet. The delaminated Ti_3C_2 nanosheet was collected from the supernatant after ultrasonication and centrifugation process, as described in the Experimental

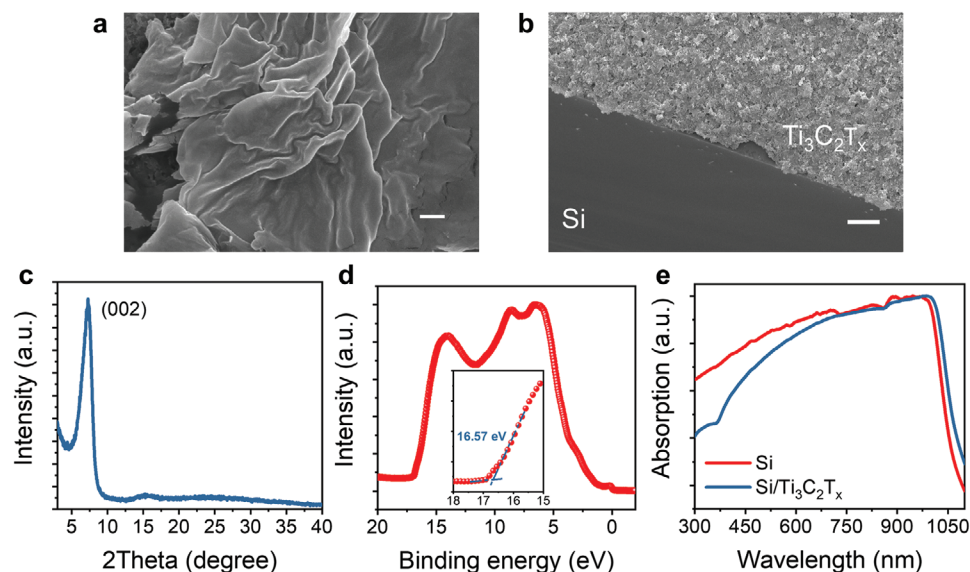


Figure 1. Microstructure morphologies, X-ray diffraction (XRD), ultraviolet photoelectron spectroscopy (UPS), and optical characterization of the Ti_3C_2 nanosheet film. Scanning electron microscope (SEM) images of a) the delaminated Ti_3C_2 nanosheet (scale bar, 200 nm) and b) spray deposited Ti_3C_2 nanosheet film on Si (cross-sectional view; scale bar, 1 μm). Corresponding c) XRD patterns, d) UPS spectrum, and e) UV-vis absorption spectrum of the as-obtained Ti_3C_2 film.

Section in detail. The as-prepared Ti_3C_2 MXene solution was then loaded onto a spray gun, ready for the fabrication of Ti_3C_2 film. Figure 1b shows the cross-sectional SEM of the as-spray deposited Ti_3C_2 film on Si. The film thickness was fine controlled by the carrier gas flux, the distance between the spray gun and the substrate and the volume of Ti_3C_2 solution. Experimentally, 80–200 μL solution was sprayed onto a $1 \times 1 \text{ cm}^2$ Si substrate. The as-fabricated MXene thin film presents flat surface (representative SEM images shown in Figure S1, Supporting Information), and their thickness was measured to be $\approx 105\text{--}267 \text{ nm}$ for 80–200 μL solution (Figure S2, Supporting Information) by a step profiler.

The X-ray diffraction (XRD) patterns shown in Figure 1c exhibits strong (002) peak located at $\approx 7.3^\circ$, which agrees well with previous literatures, further confirming the obtained Ti_3C_2 flakes with few-layered structures.^[19,20] It is only observed in the patterns the (002) peak without impure peaks due to the incomplete etching process. And the intensive peak intensity indicates highly c-oriented stacking of the spray fabricated Ti_3C_2 film.^[20] In addition, the slightly red-shifted c-lattice calculated by the (002) diffraction angle from theoretical value implies the presence of surface functional groups ($-\text{OH}$, $-\text{O}$, and $-\text{F}$), consistent with spray coated Ti_3C_2 film in previous

reports.^[21,30] According to the energy-dispersive spectroscopy mapping illustrated in Figure S3 (Supporting Information), Ti and C are the main elements, while O and F occupy a smaller portion. These surface functional groups presented between Ti_3C_2 nanosheet are in close relationship with their electronic energy band structures.^[31] The ultraviolet photoelectron spectroscopy (UPS) spectrum (Figure 1d) survey reveals that the WF of the as-obtained Ti_3C_2 film is 4.56 eV, which is calculated by subtracting the secondary electron cut-off energy from the incident ultraviolet photon energy (21.22 eV).^[32] This value is higher than previously reported value of 4.35 eV,^[22] whereas it is similar to the reported values of 4.60^[30] and 4.62 eV.^[21] The WF of Ti_3C_2 film is higher than that of n-Si, which is expected to form a Schottky barrier junction. Figure 1e illustrates the UV-vis absorption spectrum of the Ti_3C_2 film on Si. Obviously, the Ti_3C_2 film broadens the cut-off wavelengths of Si slightly in the infrared region, while the light absorption has little influence on the UV-Vis region.

Figure 2a displays the schematic structure of the $\text{Ti}_3\text{C}_2/\text{Si}$ diode. A real device picture is also presented in the inset. The interfacial SiO_x layer was grown on the Si surface in a Radio Corporation of America Standard Clean (RCA-SC-2) solution (hereafter denoted as $\text{SiO}_{x, \text{Reg}}$). It has been proved the efficacy

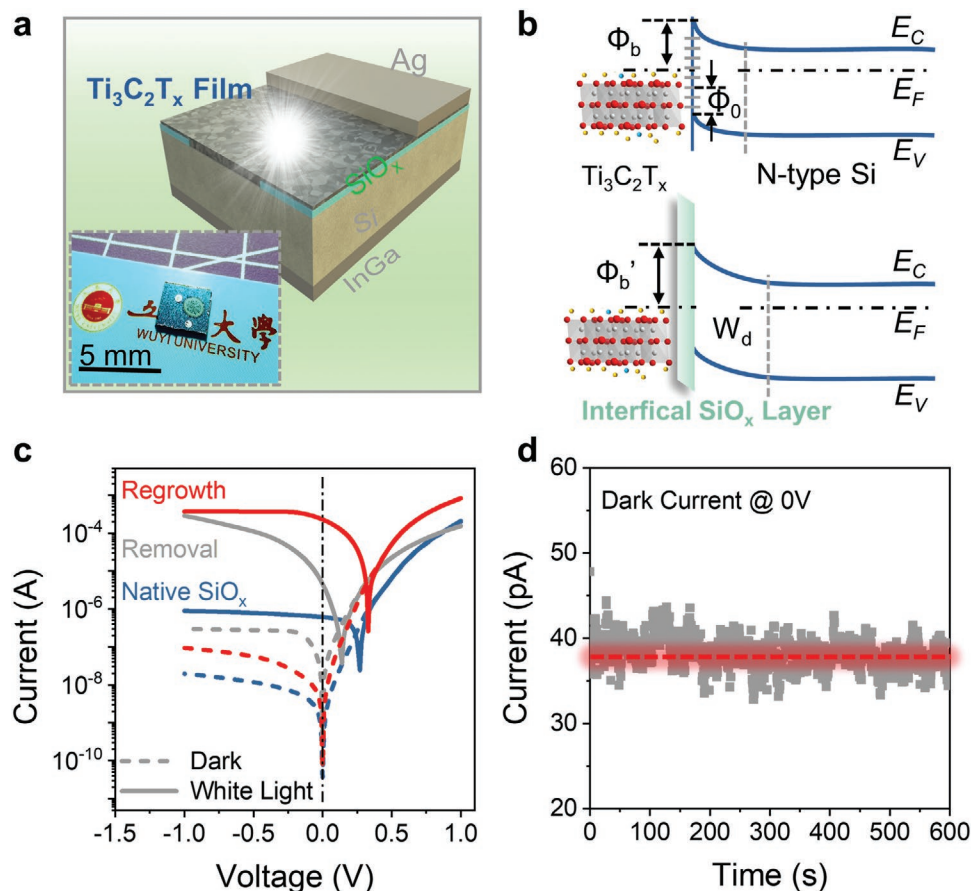


Figure 2. Photoelectric characteristics for the $\text{Ti}_3\text{C}_2/\text{Si}$ heterojunction photodiode through interfacial improvements. a) Schematic illustration of the $\text{Ti}_3\text{C}_2/\text{SiO}_x/\text{Si}$ photodetector (PD), the inset shows a real device picture. b) Energy-band diagram of a $\text{Ti}_3\text{C}_2/\text{Si}$ heterojunction before and after interfacial modification, where Φ_0 is the surface potential, W_d is the depletion width. c) I - V curves for three PDs with different interfacial layers, i.e., native SiO_x layer (blue), removal of native SiO_x layer (gray), and chemical regrowth of SiO_x layer (red). d) Dark current recorded at 0 V bias for 600 s.

in a Si photoanode for water splitting using the RCA method to regrow SiO_x interfacial layer to reduce the Fermi level pinning arising from the incomplete termination of the Si surface.^[29,33] This is of particular importance for a Schottky contact, since the barrier height is rigorously influenced by the surface potential when the Fermi level of a semiconductor is severely pinned. Figure 2b illustrates the schematic energy band diagram of Ti₃C₂/Si and Ti₃C₂/SiO_{x, Reg}/Si heterojunctions. When the Ti₃C₂ (WF of 4.56 eV) film is in contact with n-Si, it forms a Schottky energy barrier, resulting in electrons flow from the Si into Ti₃C₂ and leaving in a depletion region in the Si side. The energy band then bends upward in the heterojunction interface to create a built-in electric field that is dependent on the WF difference between Ti₃C₂ and Si. However, in a real device the relatively high density of surface states is presented at the Si surface, which pins the surface Fermi level and increases interface charge recombination. As a result, the dark leakage current is substantially increased and photocurrent is remarkably reduced, which severely ruins the responsivity and detectivity of a PD. When an interfacial SiO_x is presented at the heterojunction interface, it serves as a blocking layer to suppress the dark leakage. Upon light illumination, light generated electron-hole pairs in the Si are separated via the built-in field at the MXene/Si interface. Then holes are pulled toward the MXene through tunneling the interfacial barrier while electrons are moved to the Si side and collected by the back electrode.

A comparison of dark and light current–voltage (*I*–*V*) curves plotted in Figure 2c manifests the efficacy of the introduced SiO_{x, Reg} layer. The dark current for a Ti₃C₂/Si PD without SiO_x layer with contact area of 3.14 mm² (diameter of 1 mm) are 2.7 × 10^{−7} A (at −0.3 V) and 3.1 × 10^{−10} A (at 0 V), while the values for the device with SiO_{x, Reg} are 3.4 × 10^{−8} and 4.0 × 10^{−11} A, respectively. Meanwhile, the photocurrent (*I*_{ph}) is increased nearly two orders of magnitude measured with white light illumination (90 μW), indicating that the SiO_{x, Reg} layer efficiently improves the interfacial quality and remits the interface related carrier recombination. In this case, the light on/off ratio reaches an ultrahigh value of 5 × 10⁶ at 0 V bias. A high on/off ratio means a high resolution to detect signals from noise environment, which is an advantage for weak light applications. Moreover, a device with native SiO_x layer is also presented for comparison. Although the Ti₃C₂/Si PD with native SiO_x interfacial layer has lower dark current than the device with SiO_{x, Reg} layer, its photocurrent is much inferior. The interfacial improvements are further confirmed by analyzing the diode characteristics. From the dark *I*–*V* plots (see Figure S4, Supporting Information), diode parameters, idea factor (*n*), and Schottky barrier height (ϕ_b), are determined (note S1, Supporting Information). Table S1 (Supporting Information) summarizes the parameters for the three diodes. Compared to the SiO_x layer removed device, the *n* value for the device with SiO_{x, Reg} layer is reduced from 7.03 to 3.12, while the ϕ_b is slightly increased from 0.89 to 0.93 eV. It is worth noting that this calculated ϕ_b for the Ti₃C₂/SiO_{x, Reg}/Si diode is very similar to the idea value of 0.95 eV when taken the electron affinity for n-Si of 3.61 eV from literature^[22] and WF of Ti₃C₂ of 4.56 eV from the UPS result (Figure 1d). Figure 2d shows the long-term dark current measurement of the Ti₃C₂/SiO_{x, Reg}/Si photodiode, indicating a low value fluctuated around 40 pA in the tested time domain, further demonstrating the

stability of the chemically modified interface. All these data imply that the chemically regrown SiO_x on Si surface improves the interface quality and the diode characteristics.

Fundamentally, it is a trade-off for the sheet resistance and optical transmission of the Ti₃C₂ film as with increasing its thickness. Therefore, the Ti₃C₂ film thickness is adjusted to balance the photoelectric properties of the Ti₃C₂/SiO_{x, Reg}/Si heterojunction photodiode. It reveals that the Ti₃C₂ film (≈125 nm) with 100 μL colloid solution spray coated holds a better photoreponse while maintaining a low dark current (Figure S5, Supporting Information). Hereafter, this film thickness is applied to evaluate the performances of the PD. Figure 3 presents wavelength dependent photoresponse of the Ti₃C₂/SiO_{x, Reg}/Si photodiode in the range of 300–1000 nm. Figure 3a,b exhibits wavelength dependent photocurrent *I*_{ph}, external quantum efficiency *EQE*, responsivity *R*, and specific detectivity *D*^{*} recorded at 0 V. Although the *I*_{ph} at 0 V bias is slightly lower than the saturated values at reverse bias (see Figure 2c), the dark current at 0 V is far smaller due to the lack of external electrical perturbation, which guarantees an ultrahigh detectivity when considering the dark current is dominated by the shot noise. Moreover, the self-powered ability with ultralow power assumption makes the PDs promising for portable, implantable sensor networks. It is noted the photocurrent fluctuation in the range of 800–1000 nm is caused by the light power fluctuation of the test equipment. The responsivity *R* (in mA W^{−1}), external quantum efficiency *EQE*, and specific detectivity *D*^{*} (in Jones,

cm Hz^{1/2} W^{−1}) are described by the equations: $R = \frac{I_{ph} - I_d}{P_{in}}$,

$$EQE = \frac{1240}{\lambda} \times R \times 10^3 \text{ and } D^* = \frac{R\sqrt{S}}{\sqrt{2qI_d}}, \text{ respectively, where } I_d \text{ is}$$

the dark current, *P*_{in} is the incident light power, *S* is the device active area (3.14 mm²), λ is the incident wavelength, and *q* is the elementary electrical charge.^[34,35] The responsivity and *EQE* determine the sensitivity of a PD, while the specific detectivity is an assessment for the weak light signal recognition ability.^[36,37] The photocurrent *I*_{ph} is higher than 1 μA in the overall measured spectrum with a peak value of 5.8 μA at 470 nm. The high output photocurrent yields the high *EQE* values in the vis-NIR region, with *EQE* values higher than 50% in the 440–960 nm range and a maximum *EQE* of 60.3% at 540 nm. The *EQE* is decreased at short wavelengths which may due to the loss of high energy photons at the surface of Ti₃C₂ film and/or at the heterojunction interface. The responsivity and specific detectivity spectrum display a gradually increased trend with peaks of 402 mA W^{−1} and 2.03 × 10¹³ Jones at 910 nm. The observed high responsivity is probably in close relationship with a photoconductive gain underlying the bulk Si, since hole collection contributes to the photocurrent more than electrons do. Moreover, it is noted that both the peak *R* and *D*^{*} show slightly deviation from other Si based vdW heterojunction PDs such as graphene/Si,^[28] which should be attributed to the interaction between Si and Ti₃C₂ film.

I–*V* and current–time (*I*–*t*) curves under series of typical monochromatic light illumination are plotted in Figure 3c and Figure S6 (Supporting Information). It is obvious that the on/off alternative switching cycles are repeatable and reproducible. The on/off ratio is higher than 10⁵ under all the light stimuli,

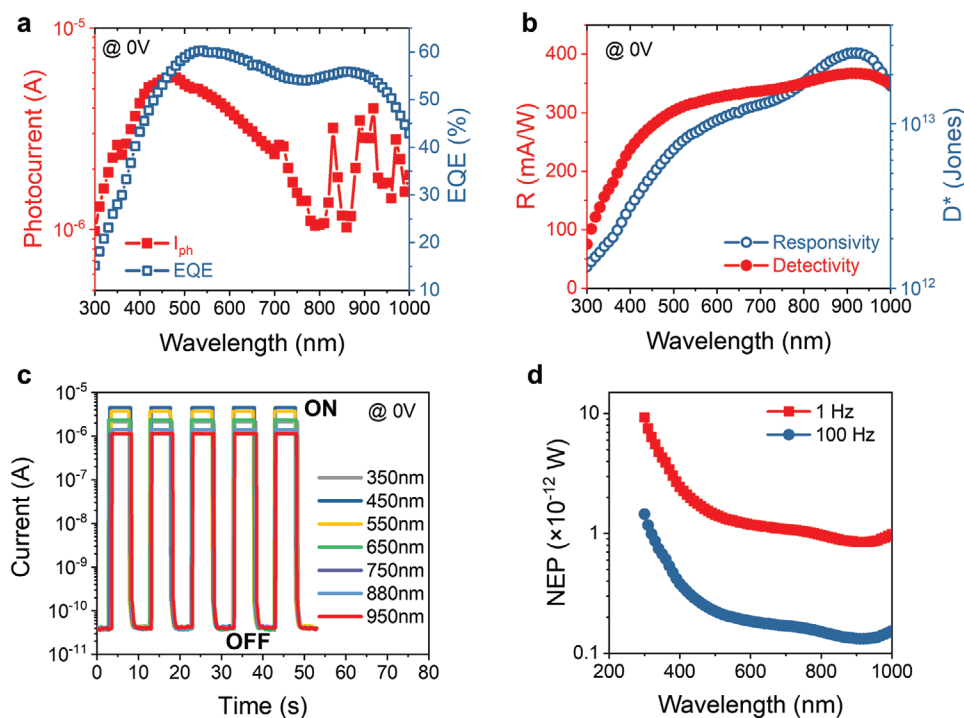


Figure 3. Photoelectric properties of the $\text{Ti}_3\text{C}_2/\text{SiO}_{x,\text{Reg}}/\text{Si}$ photodetector (PD). a) Photocurrent I_{ph} and external quantum efficiency external quantum efficiency (EQE) as a function of incident light wavelengths (300–1000 nm). b) Spectral responsivity R and specific detectivity D^* . c) I – T curves of the PD under various wavelengths of incident light. d) Noise equivalent power (NEP) as a function of light wavelengths at frequency of 1 and 100 Hz.

indicating an excellent signal-to-noise ratio. To further explore the noise equivalent power (NEP) that the PD can differentiate the minimum incident light power from noise, dark current noise density spectra was measured (Figure S7, Supporting Information). The NEP values are calculated by the equation $\text{NEP} = \frac{i_n}{R}$, where i_n is the noise current. At 0 V bias, the dark current is dominated by the thermal noise, which is inversely related to the shunt resistance of a PD. As with increasing the reversed bias, the $1/f$ noise becomes the major contributor at low frequency.^[28] Using the dark noise current (0 V) of $0.34 \text{ pA Hz}^{-1/2}$ at 1 Hz and $0.05 \text{ pA Hz}^{-1/2}$ at 100 Hz, the NEP spectrum is determined (Figure 3d). The NEP for our device shows a declined trend from 300 to 1000 nm with the minimum values of 0.85 pW (1 Hz) and 0.13 pW (100 Hz).

To further evaluate the $\text{Ti}_3\text{C}_2/\text{SiO}_{x,\text{Reg}}/\text{Si}$ photodiode, light power dependent photoresponse characteristics of the $\text{Ti}_3\text{C}_2/\text{SiO}_{x,\text{Reg}}/\text{Si}$ heterojunction PD are summarized in Figure 4. As shown in Figure 4a,b, I – V and I – t curves were recorded under incident light wavelength of 900 nm with light power increased from 0.058 to $6.93 \text{ }\mu\text{W}$. As with increasing the incident light power, the photocurrent is inclined steadily. At 0 V bias, the photocurrent keeps unchanged under continuous light illumination, implying that the PD works efficiently and stably in self-powered mode. The PD can track the light signal very well, and the photocurrent signal rises and falls rapidly as with the light switched on and off. Notably, even under a very low incident light power of 58 nW (instrumental limit), the PD exhibits a high light on/off ratio of more than three orders of magnitude. From the light power dependent

I – V data, short-circuit current and open-circuit voltage versus power are extracted and presented in Figure 4c. The short-circuit current increases directly linear with the optical power inclined from 58 nW to $6.93 \text{ }\mu\text{W}$, which indicates the photo-generation efficiency is not yet saturated in this measured optical power range. On the other hand, this linear output feature is conducive for simplifying circuit design in practical applications. Whereas the open-circuit voltage rises with light power and reaches a saturated value around 260 mV . The observed photovoltaic behavior should be the origin for the PD working under 0 V bias. Moreover, light power dependent responsivity and specific detectivity are displayed in Figure 4d. It is observed that both R and D^* maintain steadily at high values around 410 mA W^{-1} and 2.05×10^{13} Jones, respectively, with a small fluctuation as with increasing the light power. This figure-of-merit stands out within many other Si based PDs, where the R and D^* are normally decreased as with increasing the light power.^[38–42] Figure 4e compares the $\text{Ti}_3\text{C}_2/\text{SiO}_{x,\text{Reg}}/\text{Si}$ PD with previous reports on Si based heterojunction self-powered PDs.^[7,38–45] The R and D^* of commercial Si and Ge photodiodes (from Thorlabs, Inc.) are shown as well for comparison. Notably, the presented $\text{Ti}_3\text{C}_2/\text{SiO}_{x,\text{Reg}}/\text{Si}$ photodetector with high detectivity and responsivity stands out in this comparison. And it is also competitive to commercial Si and Ge based photodetectors, demonstrating that it may find applications for weak signal detecting applications.

The response speed of the PD was experimented by recording the photoresponse to a pulsed laser using a quick response measurement system to assess the accurate rise and decay time (Figure 5). Figure 5a presents 10 typical response

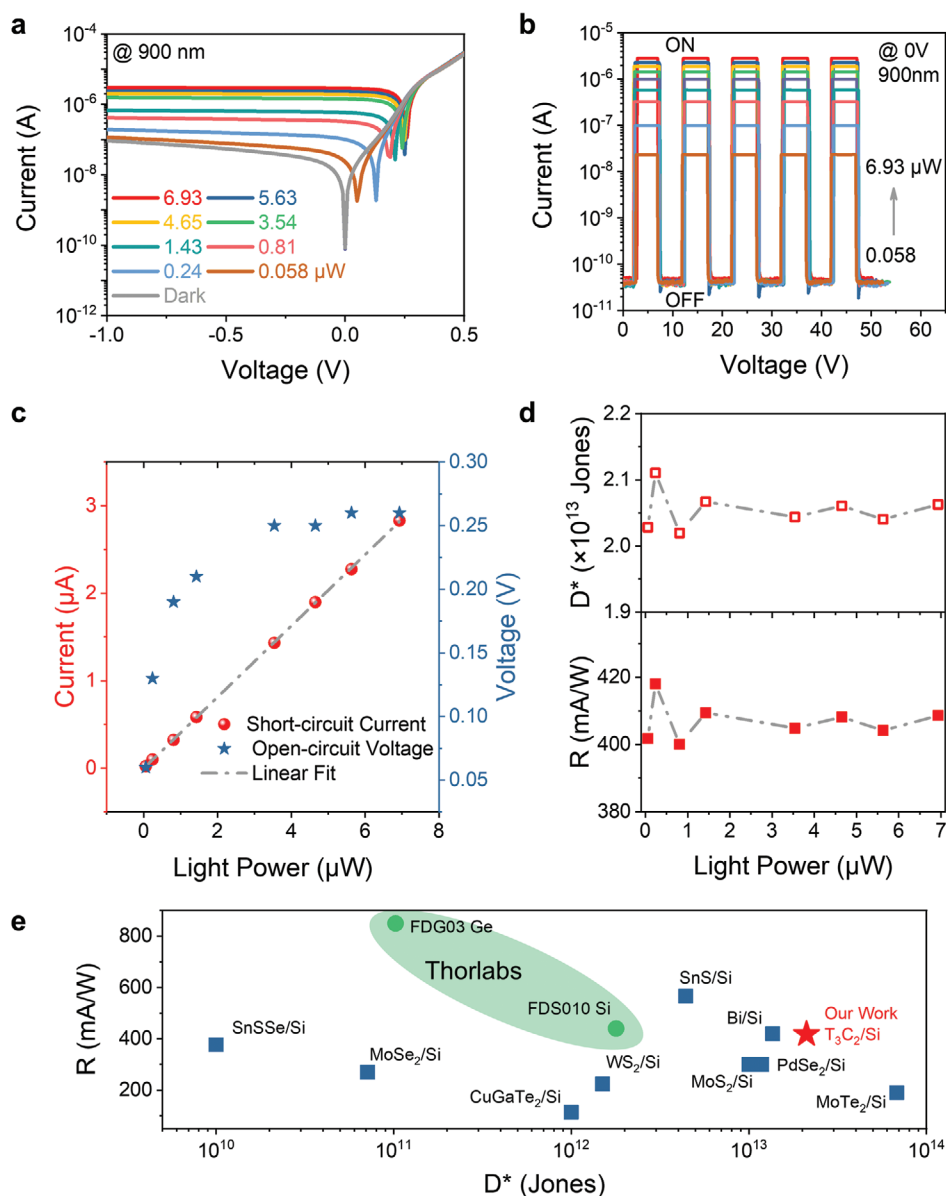


Figure 4. a) I - V and b) I - T plots of the $\text{Ti}_3\text{C}_2/\text{SiO}_{x,\text{Reg}}/\text{Si}$ photodetector (PD) under 900 nm monochromatic light illumination with series of light power (0.058–6.93 μW), where the I - T curves are recorded under 0 V bias and alternative on/off switching light. c) Light power dependent short-circuit current and open-circuit voltage. d) R and D^* as a function of light power. e) Comparison of R and D^* for our device with previous reports on Si based heterostructure PDs. The values for commercial Si and Ge PDs (Thorlabs, Inc.) are also presented for comparison.

cycles. From the magnified plot for a single response cycle (Figure 5b), the rise time τ_r and decay time τ_d of our device are found to be 0.14 and 1.6 ms, respectively. The response speed is faster than $\text{Ti}_3\text{C}_2/\text{Si}$,^[21] $\text{Ti}_3\text{C}_2/\text{perovskite}$,^[22] SnSSe/Si ^[43] heterojunction PDs in literatures, and is comparable to the graphene/Si PD,^[28] but slower than WS_2/Si ,^[41] MoS_2/Si ,^[40] MoSe_2/Si ,^[44] MoTe_2/Si ^[7] PDs. However, the solution-processable fabrication of MXene electrode is competitive for large-scale and low-cost PDs.

As a matter of fact, the long-term air stability of the Ti_3C_2 MXene is still a challenge, which significantly limits its application in optoelectronics. To this end, the fabricated $\text{Ti}_3\text{C}_2/\text{SiO}_{x,\text{Reg}}/\text{Si}$ PD was encapsulated with silicone and its

photoelectric performance was assessed and compared in Figure 6. I - V and I - t tests illustrated in Figure 6a,b reveal that the short-circuit current is slightly declined from 0.257 mA (before package) to 0.210 mA (after package) under white light (90 μW) illumination, while the repeatable on/off switching cycles with ultrahigh on/off ratio over 10^6 are maintained. Moreover, Figure 6c,d displays the R , EQE , and D^* spectra of the $\text{Ti}_3\text{C}_2/\text{SiO}_{x,\text{Reg}}/\text{Si}$ photodiode after the package. As with the photocurrent, after silicone encapsulation the peak R and EQE values are decreased to 378 mA W^{-1} and 54%, respectively, corresponding to 90% of its original values. In contrast, the peak D^* value of the packaged device has a small improvement from 2.03×10^{13} to 2.09×10^{13} Jones.

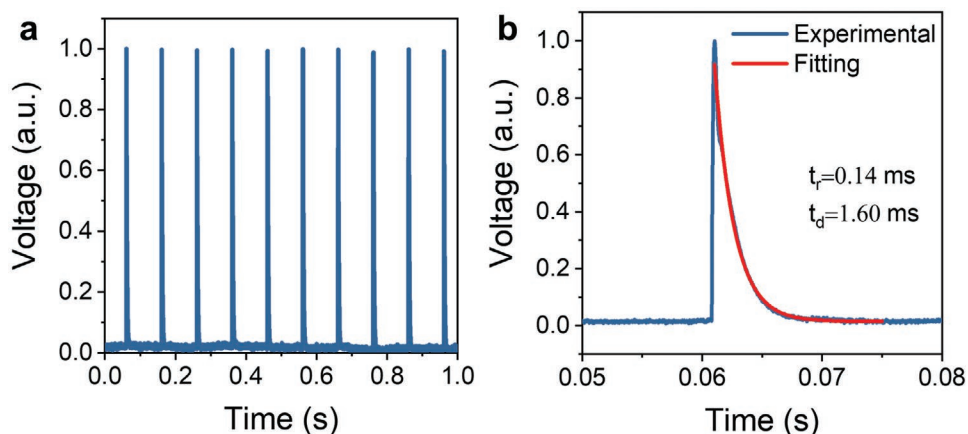


Figure 5. Response speed of the $\text{Ti}_3\text{C}_2/\text{SiO}_{x,\text{Reg}}/\text{Si}$ photodetector (PD). a) Typical pulse response of the PD to a pulse laser (532 nm, 10 Hz). b) A single pulse response extracted to evaluate the rise and decay time, where the decay process is fitted using the second-order exponential fit.

3. Conclusion

In conclusion, self-powered Ti_3C_2 MXene/Si heterojunction PDs with chemically regrown interfacial oxidized layer show much improved photoresponse and dark leakage simultaneously, due to the improved interface quality. With the chemically regrown SiO_x interfacial layer, the dark current is reduced by an order of magnitude compared to that without interfacial SiO_x layer devices, whereas the photocurrent is enhanced by two orders

of magnitude compared to that with natively oxidized interface. The improved photodetector exhibits high photodetecting performances, including an ultrahigh specific detectivity of 2.03×10^{13} Jones and a remarkable responsivity of 402 mA W^{-1} at zero external bias without noticeable decline as with increasing the light power. Moreover, the PDs show a high signal-to-noise ratio with light on/off ratio of over 10^6 , an outstanding peak *EQE* of 60.3% and rise/decay time of 0.14/1.6 ms. In addition, to isolate the Ti_3C_2 MXene from surrounding environment and

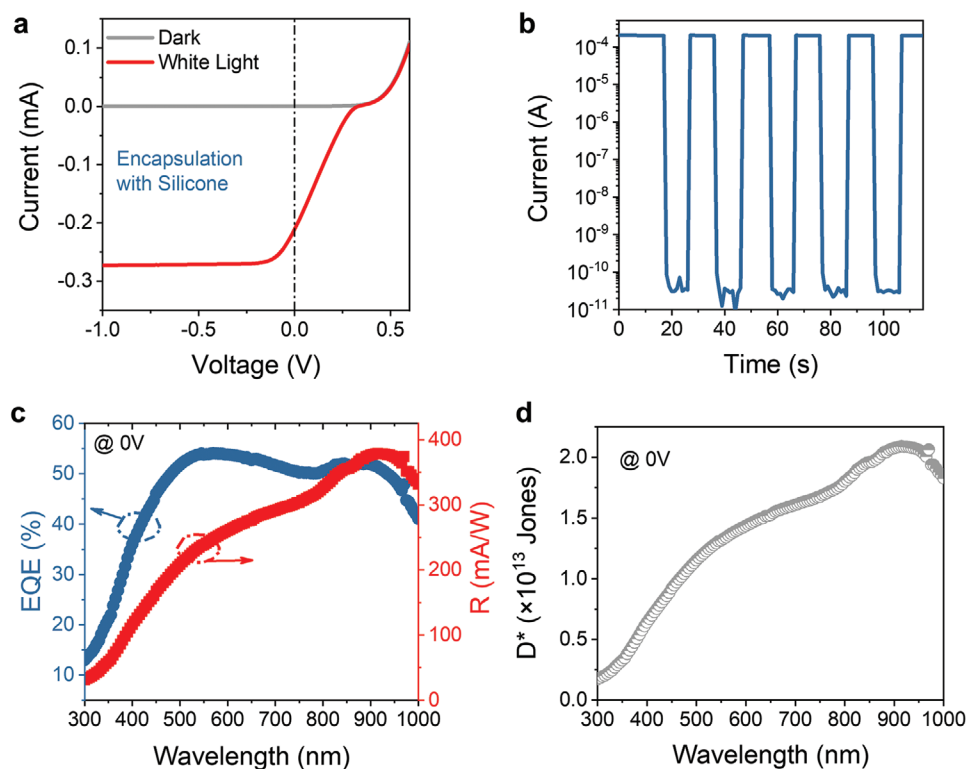


Figure 6. Photoelectric performance measurements of the $\text{Ti}_3\text{C}_2/\text{SiO}_{x,\text{Reg}}/\text{Si}$ photodetector after encapsulated with silicone. a) *I*-*V* curves in linear scale under dark and white light illumination. b) *I*-*T* plot under on/off switching light at 0 V bias. Wavelength dependent c) *EQE* (blue) and *R* (red), and d) D^* at 0 V bias.

to make the photodetector working stably, the packaged PDs with silicone still preserves highly performing, with *EQE* of 54% and specific detectivity of 2.09×10^{13} Jones. This interfacial modification demonstrates the possibility for the development of Si based weak light signal photodetectors. Besides, the Ti_3C_2 MXene/Si heterojunction PDs fabricated with facile solution processing presents high potential for large-scale, low-cost, and high-integration sensing applications.

4. Experimental Section

Materials Preparation: The N-type Si wafer (1–5 Ω cm, thickness 400 μm) with 200 nm thermally grown SiO_2 used for the fabrication of photodetectors was purchased from Suzhou Crystal Silicon Electronic & Technology Co., Ltd. The precursor few-layered Ti_3C_2 colloidal solution (5 g L^{-1}) was purchased from Jilin 11 Technology Co., Ltd. Before use, the solution was undergone an ultrasonic delamination (360 W, 1 h) in ice water and a centrifugation (4000 rpm, 20 min) process to obtain the supernatant. The final product was diluted to 1.25 g L^{-1} using deionized (DI) water, allowing for the following device fabrication. To protect the as-obtained Ti_3C_2 from potential oxidation, the liquid storage bottle was filled with argon gas and stored in a refrigerator.

Device Fabrication: The Si/ SiO_2 wafers were washed using acetone, ethanol, and DI water in sequence. To promise hydrophilic surface, the Si wafer was immersed in piranha solution (concentrated H_2SO_4 : H_2O_2 (30%) = 7:3 in volume) for several hours. A small drop of BOE solution was dropped on Si/ SiO_2 wafer to expose the Si surface, followed by rinsing using DI water and drying using N_2 gas, immediately for the deposition of Ti_3C_2 film. For the native SiO_x samples, they were stored in atmosphere over night after the removal of SiO_2 for the regrowth of SiO_x interfacial layer, whereas for the chemically grown SiO_x samples, they were regrown in an RCA SC-2 (H_2O : HCl : H_2O_2 = 5:1:1 in volume) etchant solution for 10 min at 75 $^\circ\text{C}$ to produce a thin SiO_x interfacial layer on the Si surface. The Ti_3C_2 film was prepared by a spray coating method using a spray gun with N_2 as carrier gas. The film thickness was fine controlled by maintaining the N_2 gas flow rate at 1.8 mbar and the spray distance of ≈ 10 cm, whereas the volume of Ti_3C_2 colloidal suspension was adjusted from 80 to 200 μL . After the deposition, the Ti_3C_2 /Si samples were dried in vacuum overnight. Finally, InGa eutectic was casted on Si backside for ohmic contact, while a small drop of Ag paste was dropped onto a corner of the Ti_3C_2 film and dried for probe contacting. During the photoelectrical measurements, the MXene acted as an anode, while the InGa at Si backside acted as a cathode.

Characterization and Measurements: The sample morphologies were characterized by a field-emission scanning electron microscope (Zeiss Sigma), XRD patterns were conducted on a Bruker D8 diffractometer equipped with $\text{Cu K}\alpha$ radiation ($\lambda = 1.5405 \text{ \AA}$). The transmittance/absorption spectra were experimented on an UV-vis spectrometer (Hitachi U-3900H). The film thickness was obtained by a profilometer (Bruker Dektak XT). The noise spectrum was collected by a noise measurement system (FS-Pro, Platform Design Automation Inc.). The performance measurements of the Ti_3C_2 /Si photodiode were conducted on a quantum efficiency testing system containing a precision source meter (Keithley 2612B) and a xenon arc lamp in combination with a monochromator as light sources. A Nova II power meter (OPHIR photonics) was used to calibrate the light power. The response speed of was evaluated by connection the photodetector with a 1 G Ω resistor while a 532 nm Nd:YAG pulsed laser and a digital oscilloscope (Tektronix DPO 5140B) were used as light stimuli and data collection, respectively. All these measurements were conducted under ambient conditions at room temperature.

Supporting Information

Supporting Information is available from the Wiley Online Library or from the author.

Acknowledgements

This work was supported by Key-Area Research and Development Program of Guangdong Province (2020B010174004), Guangdong Basic and Applied Basic Research Foundation (2020A1515110185), Featured Innovation Projects of Colleges and Universities in Guangdong Province (2018KTSCX232), Wuyi University-Hong Kong-Macau Joint Research and Development Fund (2019WGALH06), Key Laboratory of Optoelectronic Materials and Applications in Guangdong Higher Education (2017KSYS011), Innovative Leading Talents of Jiangmen [Jiangren (2019) 7], GDAS' Project of Science and Technology Development (2019GDASYL-0105060), and Natural Science Foundation of Guangdong Province (2018A0303130334).

Conflict of Interest

The authors declare no conflict of interest.

Data Availability Statement

Research data are not shared.

Keywords

MXene, photodetector, self-powered, Ti_3C_2 , van der Waals heterojunction

Received: January 23, 2021

Revised: March 5, 2021

Published online: April 23, 2021

- [1] J. Yao, G. Yang, *Nanoscale* **2020**, 12, 454.
- [2] Z. Zhang, P. Lin, Q. Liao, Z. Kang, H. Si, Y. Zhang, *Adv. Mater.* **2019**, 31, 1806411.
- [3] D. Jariwala, T. J. Marks, M. C. Hersam, *Nat. Mater.* **2017**, 16, 170.
- [4] F. H. Koppens, T. Mueller, P. Avouris, A. C. Ferrari, M. S. Vitiello, M. Polini, *Nat. Nanotechnol.* **2014**, 9, 780.
- [5] J. Miao, X. Liu, K. Jo, K. He, R. Saxena, B. Song, H. Zhang, J. He, M. G. Han, W. Hu, D. Jariwala, *Nano Lett.* **2020**, 20, 2907.
- [6] S. Das, D. Pandey, J. Thomas, T. Roy, *Adv. Mater.* **2019**, 31, 1802722.
- [7] Z. Lu, Y. Xu, Y. Yu, K. Xu, J. Mao, G. Xu, Y. Ma, D. Wu, J. Jie, *Adv. Funct. Mater.* **2020**, 30, 1907951.
- [8] H. P. Wang, S. Y. Li, X. Y. Liu, Z. F. Shi, X. S. Fang, J. H. He, *Adv. Mater.* **2021**, 33, 2003309.
- [9] H. Tian, A. Hu, Q. Liu, X. He, X. Guo, *Adv. Opt. Mater.* **2020**, 8, 1901741.
- [10] J. Lu, Z. Zheng, J. Yao, W. Gao, Y. Zhao, Y. Xiao, J. Li, *Small* **2019**, 15, 1904912.
- [11] R. Zhuo, L. Zeng, H. Yuan, D. Wu, Y. Wang, Z. Shi, T. Xu, Y. Tian, X. Li, Y. H. Tsang, *Nano Res.* **2019**, 12, 183.
- [12] W. Chen, R. Liang, S. Zhang, Y. Liu, W. Cheng, C. Sun, J. Xu, *Nano Res.* **2019**, 13, 127.
- [13] C. Jia, D. Wu, E. Wu, J. Guo, Z. Zhao, Z. Shi, T. Xu, X. Huang, Y. Tian, X. Li, *J. Mater. Chem. C* **2019**, 7, 3817.
- [14] X. Wan, Y. Xu, H. Guo, K. Shehzad, A. Ali, Y. Liu, J. Yang, D. Dai, C.-T. Lin, L. Liu, H.-C. Cheng, F. Wang, X. Wang, H. Lu, W. Hu, X. Pi, Y. Dan, J. Luo, T. Hasan, X. Duan, X. Li, J. Xu, D. Yang, T. Ren, B. Yu, *npj 2D Mater. Appl.* **2017**, 4, 1.
- [15] J. X. Chen, Z. L. Li, F. L. Ni, W. X. Ouyang, X. S. Fang, *Mater. Horiz.* **2020**, 7, 1828.
- [16] M. Khazaei, A. Ranjbar, M. Arai, T. Sasaki, S. Yunoki, *J. Mater. Chem. C* **2017**, 5, 2488.
- [17] H. Kim, Z. Wang, H. N. Alshareef, *Nano Energy* **2019**, 60, 179.

- [18] H. Xu, A. Ren, J. Wu, Z. Wang, *Adv. Funct. Mater.* **2020**, *30*, 2000907.
- [19] M. Ghidui, M. R. Lukatskaya, M. Q. Zhao, Y. Gogotsi, M. W. Barsoum, *Nature* **2014**, *516*, 78.
- [20] W. Tian, A. VahidMohammadi, Z. Wang, L. Ouyang, M. Beidaghi, M. M. Hamed, *Nat. Commun.* **2019**, *10*, 2558.
- [21] W. Deng, H. Huang, H. Jin, W. Li, X. Chu, D. Xiong, W. Yan, F. Chun, M. Xie, C. Luo, L. Jin, C. Liu, H. Zhang, W. Deng, W. Yang, *Adv. Opt. Mater.* **2019**, *7*, 1801521.
- [22] Z. Kang, Y. Ma, X. Tan, M. Zhu, Z. Zheng, N. Liu, L. Li, Z. Zou, X. Jiang, T. Zhai, Y. Gao, *Adv. Electron. Mater.* **2017**, *3*, 1700165.
- [23] Z. Ma, K. Ma, S. Lu, S. Wang, X. Liu, B. Li, L. Zhang, X. Wang, *Sens. Actuators A: Phys.* **2020**, *315*, 112304.
- [24] K. Montazeri, M. Currie, L. Verger, P. Dianat, M. W. Barsoum, B. Nabet, *Adv. Mater.* **2019**, *31*, 1903271.
- [25] H. C. Fu, V. Ramalingam, H. Kim, C.-H. Lin, X. S. Fang, H. N. Alshareef, J. H. He, *Adv. Energy Mater.* **2019**, *9*, 1900180.
- [26] A. M. Cowley, S. M. Sze, *J. Appl. Phys.* **1965**, *36*, 3212.
- [27] S. G. Nam, Y. Cho, M. H. Lee, K. W. Shin, C. Kim, K. Yang, M. Jeong, H. J. Shin, S. Park, *2D Materials* **2018**, *5*, 041004.
- [28] X. Li, M. Zhu, M. Du, Z. Lv, L. Zhang, Y. Li, Y. Yang, T. Yang, X. Li, K. Wang, H. Zhu, Y. Fang, *Small* **2016**, *12*, 595.
- [29] I. A. Digdaya, G. W. P. Adhyaksa, B. J. Trzesniewski, E. C. Garnett, W. A. Smith, *Nat. Commun.* **2017**, *8*, 15968.
- [30] Z. Wang, H. Kim, H. N. Alshareef, *Adv. Mater.* **2018**, *30*, 1706656.
- [31] T. Schultz, N. C. Frey, K. Hantanasirisakul, S. Park, S. J. May, V. B. Shenoy, Y. Gogotsi, N. Koch, *Chem. Mater.* **2019**, *31*, 6590.
- [32] L. Zhang, Y. Li, X. Li, C. Li, R. Zhang, J. J. Delaunay, H. Zhu, *Nano Energy* **2016**, *28*, 135.
- [33] X. Zhou, R. Liu, K. Sun, D. Friedrich, M. T. McDowell, F. Yang, S. T. Omelchenko, F. H. Saadi, A. C. Nielander, S. Yalamanchili, K. M. Papadantonakis, B. S. Brunschwig, N. S. Lewis, *Energy Environ. Sci.* **2015**, *8*, 2644.
- [34] Y. Sun, W. Song, F. Gao, X. Wang, X. Luo, J. Guo, B. Zhang, J. Shi, C. Cheng, Q. Liu, S. Li, *ACS Appl. Mater. Interfaces* **2020**, *12*, 13473.
- [35] W. Song, X. Wang, H. Chen, D. Guo, M. Qi, H. Wang, X. Luo, X. Luo, G. Li, S. Li, *J. Mater. Chem. C* **2017**, *5*, 11551.
- [36] Z. Q. Li, Z. L. Li, Z. F. Shi, X. S. Fang, *Adv. Funct. Mater.* **2020**, *30*, 2002634.
- [37] Y. Li, Z. F. Shi, W. Q. Liang, L. T. Wang, S. Li, F. Zhang, Z. Z. Ma, Y. Wang, Y. Z. Tian, D. Wu, X. J. Li, Y. T. Zhang, C. X. Shan, X. S. Fang, *Mater. Horiz.* **2020**, *7*, 530.
- [38] J. Yao, Z. Zheng, G. Yang, *ACS Appl. Mater. Interfaces* **2018**, *10*, 38166.
- [39] J. Yao, Z. Zheng, J. Shao, G. Yang, *ACS Appl. Mater. Interfaces* **2015**, *7*, 26701.
- [40] L. Wang, J. Jie, Z. Shao, Q. Zhang, X. Zhang, Y. Wang, Z. Sun, S. T. Lee, *Adv. Funct. Mater.* **2015**, *25*, 2910.
- [41] E. Wu, D. Wu, C. Jia, Y. Wang, H. Yuan, L. Zeng, T. Xu, Z. Shi, Y. Tian, X. Li, *ACS Photonics* **2019**, *6*, 565.
- [42] L. Wang, Z. Li, M. Li, S. Li, Y. Lu, N. Qi, J. Zhang, C. Xie, C. Wu, L. B. Luo, *ACS Appl. Mater. Interfaces* **2020**, *12*, 21845.
- [43] W. Gao, Z. Zheng, L. Huang, J. Yao, Y. Zhao, Y. Xiao, J. Li, *ACS Appl. Mater. Interfaces* **2019**, *11*, 40222.
- [44] J. Mao, Y. Yu, L. Wang, X. Zhang, Y. Wang, Z. Shao, J. Jie, *Adv. Sci.* **2016**, *3*, 1600018.
- [45] L. H. Zeng, D. Wu, S.-H. Lin, C. Xie, H. Y. Yuan, W. Lu, S. P. Lau, Y. Chai, L. B. Luo, Z. J. Li, Y. H. Tsang, *Adv. Funct. Mater.* **2019**, *29*, 1806878.